Available online at www.sciencedirect.com
SCIENCE DIRECT®
Journal of Computational Physics 197 (2004) 737–758
JOURNAL OF COMPUTATIONAL PHYSICS
www.elsevier.com/locate/jcp

Nonreflecting boundary conditions for the time-dependent convective wave equation in a duct

Oliver V. Atassi *

Whitney, 400 Main Street, Engineering Building M/S 162-29, East Hartford, CT 06108, USA

Received 12 March 2003; received in revised form 6 November 2003; accepted 30 December 2003
Available online 19 March 2004

Abstract

Solutions for the three-dimensional wave equation in an annular duct are represented in terms of Fourier–Bessel modes, each obeying a one-dimensional dispersive wave equation. An exact nonreflecting boundary condition, nonlocal in time but local in space, is derived for each mode. Since, in most applications, the number of propagating modes is a small finite subset of all the modes, the present condition yields a computationally efficient scheme. Convergence of the solution depends on the radial eigenvalues which characterize the dispersion of the propagating duct modes. For periodic forcing, convergence analysis shows that the solution tends toward its asymptotic limit as the reciprocal of the square root of time. Near a duct mode cut-on, the computational time required for convergence is proportional to the reciprocal of the square of the group velocity. The boundary condition is implemented numerically and tested by computing the propagation of dispersive waves with various frequencies and comparing the results with the analytic solution. Two local boundary conditions are also implemented and their performance relative to the nonlocal boundary condition is studied. Significant improvements in accuracy are observed by using the present boundary condition near cut-on. Numerical results also show that the rate of convergence of the solution to a time-periodic solution significantly decreases as the group velocity of the incident waves becomes small, consistent with the analytic results.

1. Introduction

In many applications, such as aeroacoustics and structural vibrations, the flow domain is characterized by a finite source region where complex flow-structure interactions occur and an unbounded propagation region. In order to complete the formulation of the associated initial-value-problem and specify the correct solution, a causality condition is applied at infinity. For numerical solutions, the computational domain is finite and bounded by artificial surfaces along which nonreflecting boundary conditions must be applied to satisfy the causal condition at infinity. For external problems, the inflow/outflow boundary encloses the entire flow domain. Engquist and Majda [1,2] derived an exact nonreflecting boundary condition for the

* Corresponding author.
E-mail addresses: atassio@pweh.com, oliver@eurus2.us.es (O.V. Atassi).

0021-9991/$ - see front matter © 2004 Elsevier Inc. All rights reserved.
doi:10.1016/j.jcp.2003.12.021

two-dimensional wave equation in an external domain consisting of the half-space, $x \geqslant 0$. They showed that the exact boundary condition is nonlocal in both space and time because it requires information over all of space and time. In order to derive a more practical condition, they derived a series of local approximations to the exact condition. Bayliss and Turkel [3] generalized the Sommerfeld radiation condition and derived a series of local boundary conditions based on the asymptotic solution to the wave equation in cylindrical and spherical domains. The accuracy of their conditions depends upon the distance to the boundary being large relative to the dimensions of the source region. Grote and Keller [6] derived an exact boundary condition for the three-dimensional wave equation by representing the solutions at the outer spherical boundary in terms of spherical harmonics. For solutions with a finite number of spherical harmonics, they showed that their exact condition is local in both space and time. These local conditions take advantage of the nondispersive character of waves propagating in external domains.

Thompson [4,5] developed and applied nonreflecting boundary conditions to hyperbolic systems such as the Euler equations by utilizing the method of characteristics. These boundary conditions are exact for nondispersive waves in one dimension and work well for those waves which propagate in a direction normal to the boundary but are totally reflective for waves which are nearly parallel to the outflow boundary. Applying the methodology of Engquist and Majda to the two-dimensional linearized Euler equations, Giles [8] derived approximate local boundary conditions for the inflow/outflow boundaries. More recently, several authors [10–14] have derived, a series of increasingly accurate local boundary conditions for the linearized Euler equations and have examined the effects of discretization on the inflow/outflow conditions. Although the accuracy of these conditions improves with the order of the expansion, they all become highly reflective for waves which propagate nearly parallel to the outflow boundary.

Relatively little work has focused on time-dependent boundary conditions for internal geometries such as circular or annular ducts. These problems are characterized by dispersive waves due to the presence of solid boundaries. Exact boundary conditions in two and three dimensions have been derived for time-harmonic problems where the dominant frequency is known a priori [7–9,15]. In this case, exact conditions are derived utilizing an eigenfunction expansion for the pressure and a convection condition for the other flow variables [9,15]. The advantage of this approach is that the pressure is continuous, even across wakes. Moreover, even at high frequencies, there is only a finite number of propagating modes, the remainder of the spectrum represents evanescent modes. Thus only a small number of eigenmodes are needed to represent the pressure field very accurately.

Although many problems of practical interest are characterized by a dominant frequency which is known a priori, there are situations where this does not apply and, as a result, accurate nonreflecting boundary conditions to the time-dependent wave equation need to be derived and implemented. Hagstrom and Goodrich [18,19] have derived exact nonlocal boundary conditions to the wave equation and recent work has examined local approximations to the nonlocal time operator which are computationally efficient for implementation [20,21]. In the present paper, we extend the work of [9,15] to the time domain by representing the solutions in terms of Fourier–Bessel modes and then we derive and implement an exact nonreflecting boundary condition for the time-dependent modal wave equation. As in the boundary conditions of Engquist and Majda [1] and Hagstrom [18], the condition is nonlocal in time. However, it is local in space; its nonlocal space dependence is transferred to the Fourier–Bessel space. Since for most cases a finite number of modes can accurately represent the pressure field, our formulation reduces the space dependence dimension of the boundary condition to a small finite number, leading to a compuatationally efficient scheme. In Section 2, we formulate the initial-boundary-value problem. In Section 3, we show that the three-dimensional wave equation can be reduced to a series of one-dimensional dispersive wave equations. In Section 4, we derive an exact nonreflecting boundary condition which is nonlocal in time. The nonlocal time operator is shown to be equivalent to Hagstrom's condition [18]. We then apply our condition to time-periodic waves and analytically determine the rate of convergence to a time-periodic state. In Section 5, we implement the boundary conditions in a numerical scheme and compare the convergence and

accuracy of the nonlocal boundary conditions with the local conditions of Engquist and Majda [1]. In Section 6, the numerical results are discussed.

2. Formulation

In many problems involving fluid–structure interaction, flow nonlinearities and nonuniformities are confined to a local region which we denote as the inner region, V_i. Outside of the inner region there are two outer regions, V, where the flow can be adequately described by a small perturbation to a uniform mean flow, $U_\pm$, where the subscripts $\pm$ denote the mean flow in the downstream and upstream outer regions, respectively. The outer region extends to $\infty(-\infty)$ downstream (upstream) of the inner region. For a non-heat conducting isentropic flow, the linearized Euler equations can be cast in the outer region as the convective wave equation

$$\left(\frac{D_0^2}{Dt^2} - c^2\nabla^2\right)p(\vec{x},t) = 0, \quad \vec{x} \in V, \tag{2.1}$$

where

$$\frac{D_0}{Dt} \equiv \frac{\partial}{\partial t} + U\frac{\partial}{\partial x},$$

where c is the speed of sound and the subscripts $\pm$ have been dropped for simplicity.

The objective of the present paper is to derive and numerically implement exact nonreflecting boundary conditions for (2.1) in an annular duct geometry. We introduce the cylindrical coordinates, (x, r, θ) in the axial, radial and circumferential directions, respectively. For simplicity, we consider impermeable boundary conditions at the hub and tip of the annular duct

$$\frac{\partial p}{\partial r} = 0, \quad r = r_h, r_t. \tag{2.2}$$

The initial conditions for (2.1) are given by

$$p(\vec{x},0) = c^{(1)}(\vec{x}), \quad \frac{\partial p(\vec{x},0)}{\partial t} = c^{(2)}(\vec{x}) \ \vec{x} \in V. \tag{2.3}$$

Note that often the precise initial conditions for an application are not known. Fortunately, the influence of the initial conditions on the solution diminishes with time and, in what follows, we consider their influence on the long time solution to be negligible. In order to complete the formulation of the initial-boundary-value problem, a physical causality condition must be added at infinity. This condition states that the energy associated with the waves must propagate away from the source to infinity.

We nondimensionalize the length, velocity and time with respect to the tip radius, r_t, the speed of sound, c and c/r_t, respectively. Thus the convective operator becomes

$$\frac{D_0}{Dt} \equiv \frac{\partial}{\partial t} + M_x\frac{\partial}{\partial x},$$

where M_x corresponds to the axial Mach number in aeroacoustic applications.

For computation, the numerical solution is obtained in the inner region, V_i. This region is truncated to a finite length which is bounded by two cross sections, $\partial V^\pm$. The outer regions denoted by, V, extend to plus and minus infinity. A schematic of the flow domain is shown in Fig. 1. The figure shows the infinite outer region, V, where the wavy lines in the figure are meant to denote that the outer boundary, $\partial V_\infty^\pm$ extends to

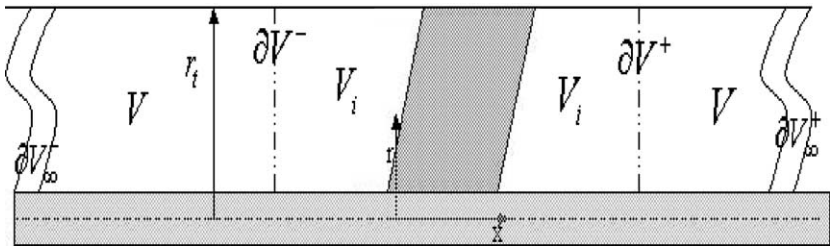

Fig. 1. Schematic of the computational domain.

$\pm\infty$. Analytical solutions in the outer region which satisfy causality are then used to obtain nonreflecting boundary conditions at $\partial V_\pm$. This restricts the class of solutions to those where the energy propagates out of the inner domain. To model noise sources which lie outside the inner regions, a condition may be imposed at both boundaries, $\partial V_\pm$, which represent incident waves propagating into the inner region. We further seek to derive nonreflecting boundary conditions involving only first-order derivatives

$$B_i p^- = 0, \quad B_e p^+ = 0, \quad \vec{x} \in \partial V^\pm, \tag{2.4}$$

where i and e denote the inlet and exit of the inner domain, respectively. The system ((2.1)–(2.4)) results in an initial-boundary-value problem whose solution coincides in V with the infinite domain problem.

3. Reduction to the one-dimensional wave equation

We assume $p(\mathbf{x}, t)$ can be uniformly expanded in terms of the annular duct eigenfunctions

$$p(x, r, \theta, t) = \sum_{n=1}^{n=\infty} \sum_{m=-\infty}^{m=\infty} p_{mn}(x, t)\, \mathrm{e}^{\mathrm{i}m\theta} R_{mn}(r), \tag{3.5}$$

where the Fourier–Bessel coefficient, p_{mn}, is given by

$$p_{mn}(x, t) = \frac{1}{2\pi \Lambda_{mn}} \int_{r_h}^{1} \int_{0}^{2\pi} r \bar{R}_{mn}(r)\, \mathrm{e}^{-\mathrm{i}m\theta} p(x, r, \theta, t)\, \mathrm{d}\theta\, \mathrm{d}r, \tag{3.6}$$

where

$$\Lambda_{mn} = \int_{r_h}^{1} r |R_{mn}|^2\, \mathrm{d}r$$

and the orthogonal eigenfunctions, $R_{mn}(r)$, are a combination of Hankel functions [16]

$$R_{mn}(r) = H_m^{(1)}(\lambda_{mn} r) - \frac{\mathrm{d}H_m^{(1)}(\lambda_{mn} r_h)/\mathrm{d}r}{\mathrm{d}H_m^{(2)}(\lambda_{mn} r_h)/\mathrm{d}r} H_m^{(2)}(\lambda_{mn} r), \tag{3.7}$$

where λ_{mn} is the eigenvalue associated with the radial eigenfunction, R_{mn}. The eigenvalue is determined by the condition

$$\begin{vmatrix} H_m'^{(1)}(\lambda_{mn} r_h) & H_m'^{(2)}(\lambda_{mn} r_h) \\ H_m'^{(1)}(\lambda_{mn}) & H_m'^{(2)}(\lambda_{mn}) \end{vmatrix} = 0. \tag{3.8}$$

For a circular duct,

$$r_h = 0, \quad \lim_{r_h \to 0} \frac{H_m'^{(1)}(\lambda_{mn} r_h)}{H_m'^{(2)}(\lambda_{mn} r_h)} = -1, \quad R_{mn} \to 2J_m(\lambda_{mn} r)$$

and (3.8) reduces to

$$J_m'(\lambda_{mn}) = 0. \tag{3.9}$$

Substituting (3.5) into (2.1) we obtain a one-dimensional dispersive wave equation for each mode $p_{mn}(x,t)$

$$\left(\frac{D_0^2}{Dt^2} - \frac{\partial^2}{\partial x^2} + \lambda_{mn}^2 \right) p_{mn}(x,t) = 0. \tag{3.10}$$

We have reduced the problem to a series of one-dimensional, convected wave equations for each Fourier–Bessel coefficient. If we introduce a combination of the Lorentz and Prandtl–Glauert transformation, $\tilde{\mathbf{x}} = \{\beta(x - M_x t), r, \theta\}$, $\tilde{t} = \beta t$ and $\tilde{\lambda}_{mn} = \lambda_{mn}/\beta$, where $\beta^2 = 1 - M_x^2$, we obtain the one-dimensional dispersive wave equation

$$\left[\frac{\partial^2}{\partial \tilde{t}^2} - \frac{\partial}{\partial \tilde{x}^2} + \tilde{\lambda}_{mn}^2 \right] p_{mn}(\tilde{x}, \tilde{t}) = 0. \tag{3.11}$$

Eq. (3.11) is also known as the telegraph equation. In order to derive a nonreflecting boundary condition, we must find an outgoing solution to (3.11). In the next section, we derive an exact nonreflecting boundary condition for (3.11) and for simplicity of notation we drop the tildes.

4. Derivation of an exact boundary condition

The reduced initial boundary value problem takes the form

$$\left[\frac{\partial^2}{\partial t^2} - \frac{\partial^2}{\partial x^2} + \lambda_{mn}^2 \right] p_{mn}(x,t) = 0, \tag{4.12}$$

and is subject to the initial conditions

$$p_{mn}(x,0) = c_{mn}^{(1)}(x), \quad \frac{\partial p_{mn}(x,0)}{\partial t} = c_{mn}^{(2)}(x), \tag{4.13}$$

where $c_{mn}^{(1)}, c_{mn}^{(2)}$ are the Fourier–Bessel coefficients of c_1, c_2 and the nonreflecting boundary conditions at the inlet and exit of the inner domain

$$B_{\mathrm{i}} p_{mn}(x_{\mathrm{i}}, t) = 0, \quad B_{\mathrm{e}} p_{mn}(x_{\mathrm{e}}, t) = 0, \tag{4.14}$$

where $x = x_{\mathrm{i}}$ lies at ∂V_- and $x = x_{\mathrm{e}}$ lies at ∂V_+.

In what follows, we derive the expressions for $B_{\mathrm{i}}, B_{\mathrm{e}}$. We define the Laplace transform of the Fourier–Bessel coefficient, p_{mn}, as

$$\mathscr{L} p_{mn} = \hat{p}_{mn}(x,s) = \int_0^\infty \mathrm{e}^{-st} p_{mn}(x,t)\, \mathrm{d}t. \tag{4.15}$$

Substituting (4.15) into (4.12), (4.13) and Eq. (4.12) takes the form,

$$\frac{\mathrm{d}^2\hat{p}_{mn}}{\mathrm{d}x^2} - (\lambda_{mn}^2 + s^2)\hat{p}_{mn} = -(sc_{mn}^{(1)}(x) + c_{mn}^{(2)}(x)). \tag{4.16}$$

Note that $c_{mn}^{(1)}, c_{mn}^{(2)}$ depend upon the initial condition used. Since the initial conditions depend upon the particular application and, in many cases, the long-time solution is independent of the initial conditions, we consider only the homogeneous solution.

The homogeneous solution is

$$\hat{p}_{mn} = \frac{\tilde{A}(s)}{\sqrt{\lambda_{mn}^2 + s^2}}\,\mathrm{e}^{-(\lambda_{mn}^2+s^2)^{1/2}(x-x_0)} + \frac{\tilde{B}(s)}{\sqrt{\lambda_{mn}^2 + s^2}}\,\mathrm{e}^{(\lambda_{mn}^2+s^2)^{1/2}(x-x_0)}, \tag{4.17}$$

where $x_0 = (x_\mathrm{i}, x_\mathrm{e})$ is the location of the inflow/outflow boundary. In order to obtain finite solutions for $|x| \to \infty$ we require $\tilde{B}(s) = 0$ for $(x - x_\mathrm{e}) > 0$ and $\tilde{A}(s) = 0$ for $(x - x_\mathrm{i}) < 0$. Note that the inverse Laplace transform,

$$\mathscr{L}^{-1}\left\{\frac{\mathrm{e}^{-\sqrt{s^2+\lambda_{mn}^2}|x-x_0|}}{\sqrt{s^2+\lambda_{mn}^2}}\right\} = H(t - |x - x_0|)J_0(\lambda_{mn}\sqrt{t^2 - (x-x_0)^2}), \quad x \geqslant x_0 \tag{4.18}$$

where H is the Heaviside function [17]. Using the convolution theorem,

$$\mathscr{L}\left\{\int_0^t p_1(\tau)p_2(t-\tau)\,\mathrm{d}\tau\right\} = \hat{p}_1(s)\hat{p}_2(s) \tag{4.19}$$

the expressions for the downstream and upstream homogeneous solutions are

$$p_{mn}^{+}(x,t) = \int_0^{t-(x-x_\mathrm{e})} a^{+}(t')J_0(\lambda_{mn}\sqrt{(t-t')^2 - (x-x_\mathrm{e})^2})\,\mathrm{d}t', \quad x > x_\mathrm{e}, \tag{4.20}$$

$$p_{mn}^{-}(x,t) = \int_0^{t-(x_\mathrm{i}-x)} a^{-}(t')J_0(\lambda_{mn}\sqrt{(t-t')^2 - (x_\mathrm{i}-x)^2})\,\mathrm{d}t', \quad x < x_\mathrm{i}. \tag{4.21}$$

The functions $a^{\pm}$ are the inverse Laplace transforms of $\tilde{A}(s)$ and $\tilde{B}(s)$, respectively. They will now be determined in terms of the first-order derivatives of the pressure. Note that

$$\frac{\partial p_{mn}^{+}}{\partial x} = -a^{+}(t - (x - x_\mathrm{e})) + \lambda_{mn}(x - x_\mathrm{e})\int_0^{t-(x-x_\mathrm{e})} a^{+}(t')\frac{J_1(\lambda_{mn}\sqrt{(t-t')^2 - (x-x_\mathrm{e})^2})}{\sqrt{(t-t')^2 - (x-x_\mathrm{e})^2}}\,\mathrm{d}t', \quad x > x_\mathrm{e} \tag{4.22}$$

$$\frac{\partial p_{mn}^{-}}{\partial x} = a^{-}(t - (x_\mathrm{i} - x)) - \lambda_{mn}(x_\mathrm{i} - x)\int_0^{t-(x_\mathrm{i}-x)} a^{-}(t')\frac{J_1(\lambda_{mn}\sqrt{(t-t')^2 - (x_\mathrm{i}-x)^2})}{\sqrt{(t-t')^2 - (x_\mathrm{i}-x)^2}}\,\mathrm{d}t', \quad x < x_\mathrm{i}. \tag{4.23}$$

Hence

$$\frac{\partial p_{mn}^{\pm}}{\partial x} = \mp a(t), \quad x = x_\mathrm{e}, x_\mathrm{i}. \tag{4.24}$$

Substituting (4.24) into (4.20) and (4.21), we obtain conditions at $x_0 = x_i, x_e$,

$$p_{mn}(x_0,t) = \mp \int_0^t \left(\frac{\partial p_{mn}}{\partial x}\right)_{x_0} J_0[\lambda_{mn}(t-t')]\,\mathrm{d}t'. \tag{4.25}$$

where the minus (plus) implies $x_0 = x_e (x_0 = x_i)$. Eq. (4.25), provides the closure conditions for the initial-boundary-value problems ((4.12)–(4.14)). We note that (4.25) is nonlocal in time. It is, however, *local* in space. Thus the nonlocal space dependence of the total pressure, p, defined in (3.5) has been replaced by the modes (mn) in the Fourier–Bessel space. However, since the propagating waves in a duct often consist of a small finite subset of all the modes, the dimension of the condition space dependence for the total pressure is reduced significantly. This results in a considerable saving of computational time leading to an efficient computational scheme.

We can express the boundary condition in a form similar to that of the method of characteristics and other local boundary conditions. We differentiate (4.25) with respect to time and, after rearrangement, we obtain an exact nonreflecting boundary condition involving first-order derivatives of the form

$$\left(\frac{\partial p^{\pm}_{mn}}{\partial t}\right)_{x_0,t} \pm \left(\frac{\partial p^{\pm}_{mn}}{\partial x}\right)_{x_0,t} = \pm\lambda_{mn}\int_0^t \left(\frac{\partial p^{\pm}_{mn}}{\partial x}\right)_{x_0} J_1\big(\lambda_{mn}(t-t')\big)\,\mathrm{d}t', \tag{4.26}$$

where the plus (minus) implies $x_0 = x_e$ $(x_0 = x_i)$. This form is similar to a relationship derived by Hagstrom [18]. Note that for nondispersive waves $\lambda_{mn} = 0$ and we obtain the usual characteristic condition,

$$\frac{\partial p^{\pm}_{mn}}{\partial t} \pm \frac{\partial p^{\pm}_{mn}}{\partial x} = 0. \tag{4.27}$$

Eq. (4.26) is a convenient analytical form for the boundary conditions because it shows the additional term resulting from the dispersive nature of the problem and illustrates the difference between the exact boundary condition and the often used characteristic boundary condition. Moreover, it shows that the characteristic boundary conditions (4.27) and other local boundary conditions are not exact for dispersive problems. This condition involves a time history of the derivative at the boundary. This is a consequence of the property that dispersive waves travel with different phase speeds and thus information at the inflow boundary will reach the outflow boundary at different times depending upon the wavelength of the acoustic wave. Since most problems march in time from an arbitrary initial state, the boundary derivatives may not be smooth for t small. To avoid this difficulty, we consider an alternate form of the boundary conditions for subsequent numerical implementation.

4.1. Modified boundary condition for numerical implementation

The form of the boundary conditions in (4.25) is convenient for numerical implementation because the spatial derivatives are integrated over time. This is useful because the spatial derivative at the exit boundary can be inaccurate for small t if the initial condition is not sufficiently smooth and lead to numerical instabilities. It is convenient for numerical implementation to express the wave Eq. (4.12) in terms of a system of first-order equations. We write (4.12) in the form of two first-order equations:

$$\begin{aligned} &\frac{\partial p^{\pm}_{mn}}{\partial t} \pm \frac{\partial p^{\pm}_{mn}}{\partial x} = \phi^{\pm}_{mn}, \\ &\frac{\partial \phi^{\pm}_{mn}}{\partial t} \mp \frac{\partial \phi^{\pm}_{mn}}{\partial x} + \lambda^2_{mn} p^{\pm}_{mn} = 0. \end{aligned} \tag{4.28}$$

Using (4.28) to express $\partial p^{\pm}_{mn}/\partial x$ in terms of $\phi^{\pm}_{mn}$ and $\partial p^{\pm}_{mn}/\partial t$, substituting the expression in (4.25), integrating by parts, and assuming $p^{\pm}_{mn}(0) = 0$, we obtain

$$\int_0^t \{\phi^{\pm}_{mn}(t')J_0[\lambda_{mn}(t-t')] + \lambda_{mn}p^{\pm}_{mn}(t')J_1[\lambda_{mn}(t-t')]\}\,\mathrm{d}t' = 0. \tag{4.29}$$

These boundary conditions are convenient for numerical implementation since the variables ϕ, p_{mn} are obtained directly from the numerical scheme described in (Section 5.1).

We have derived boundary conditions so that the solution to the wave equation is equivalent to the infinite domain problem where $\{|x_i|, |x_e|\} \to \infty$. We now show that the solution is unique. The proof is similar to that of [22] and is given in Appendix A. The above results can be summarized by the following theorem.

Theorem 1. *If the initial value problem to the wave equation in the infinite domain has a unique smooth solution, then so does the initial-boundary-value problem with the boundary condition,* 4.29*, for each mode. The two solutions coincide in* V_i.

4.2. Convergence analysis for time-harmonic problems

Here we consider problems with time-periodic forcing at the inlet plane. These problems are convenient for studying the effectiveness of the nonreflecting boundary conditions and the numerical scheme since we can derive the analytic solution and compare it to the numerical solution. In what follows, we examine the convergence of (4.25) for time-periodic solutions. We first note that an oscillatory solution of the initial-boundary-value problem ((4.12)–(4.14)) will be reached in the limit as $t \to \infty$. It is therefore important to establish how the solution reaches its asymptotic value since this will determine how fast the numerical solution will converge to its time-periodic solution. In addition, the time-dependent problem has transient solutions. Hence, the convergence to a periodic solution depends on the rate of decay of the transient waves.

Due to the linearity of the equations at the inlet and exit boundaries we can, without loss of generality, consider a single harmonic forcing whose analytical solution is of the form

$$p^{\pm}_{mn} = \mathrm{e}^{\mathrm{i}(k^{\pm}_{mn}x - \omega t)}, \tag{4.30}$$

where $k^{\pm}_{mn} = \pm\sqrt{\omega^2 - \lambda^2_{mn}}$ and the plus (minus) sign is chosen based on downstream (upstream) energy propagation. Note that when $\omega^2 > \lambda^2_{mn}$, $k^{\pm}_{mn}$ is real and the solutions correspond to propagating waves which carry acoustic energy and represent acoustic modes. When $\omega^2 < \lambda^2_{mn}$, $k^{\pm}_{mn}$ is imaginary and the branch $k^{\pm}_{mn} = \pm\mathrm{i}\sqrt{\lambda^2_{mn} - \omega^2}$ is chosen to eliminate the downstream (upstream) propagating growing solutions. The remaining evanescent modes decay exponentially as they propagate and do not carry any acoustic energy. For a given frequency, ω, there is a finite number of acoustic modes. The decay rate of the evanescent modes increases with their circumferential and radial mode orders (mn) and as a result, a truncated representation of the modal expansion consisting of the acoustic modes with a few weakly decaying evanescent modes [9,15] can be used with great accuracy at the inlet/outlet boundaries of the computational domain.

The analysis is carried out for the case of time-periodic forcing, $p_{mn} = \exp(-\mathrm{i}\omega t)$, at the inlet, $x_i = 0$. The objective of the analysis is to determine the convergence of numerical solutions to time periodic solutions. The right-hand side of (4.26) can be cast as

$$+\mathrm{i}\,\mathrm{e}^{+\mathrm{i}k_{mn}x_0}I(t,\omega,\lambda_{mn}),$$

where

$$I(t,\omega,\lambda_{mn}) = \lambda_{mn}\sqrt{\omega^2 - \lambda^2_{mn}}\int_0^t \mathrm{e}^{-\mathrm{i}\omega t'}J_1(\lambda_{mn}(t-t'))\,\mathrm{d}t', \tag{4.31}$$

where it should be understood that the + superscript has been dropped on k_{mn} for convenience. For small t, the integral $I(t,\omega,\lambda_{mn})$ is very small and (4.26) shows that $k_{mn} \approx \omega$. The solution is modified as t increases and in the limit as $t \to \infty$,

$$I(t,\omega,\lambda_{mn}) = \left(\sqrt{\omega^2 - \lambda_{mn}^2} - \omega\right) \mathrm{e}^{-\mathrm{i}\omega t}, \tag{4.32}$$

which yields the exact relation $k_{mn} = \sqrt{\omega^2 - \lambda_{mn}^2}$. We can estimate the rate of convergence of the numerical scheme by examining as $t \to \infty$ the rate of convergence of the right-hand side of (4.26). This is done in Appendix B using the stationary phase method and shows that for large $\lambda_{mn}t$, we have

$$\left(\frac{\partial p_{mn}}{\partial t}\right)_{x_0,t} + \left(\frac{\partial p_{mn}}{\partial x}\right)_{x_0,t} = -\mathrm{i}\mathrm{e}^{+\mathrm{i}k_{mn}x_0}\left\{(\omega - k_{mn})\,\mathrm{e}^{-\mathrm{i}\omega t} - \frac{\lambda_{mn}}{k_{mn}}\sqrt{\frac{2}{\pi\lambda_{mn}t}}[-\mathrm{i}\omega\sin(\lambda_{mn}t - \pi/4) + \lambda_{mn}\cos(\lambda_{mn}t - \pi/4)]\right\} + \mathrm{O}\left(\frac{1}{\lambda_{mn}t}\right). \tag{4.33}$$

Eq. (4.33) shows that the rate of convergence to a time-periodic solution as implied from the boundary condition scales with the reciprocal of the square root of $\lambda_{mn}t$. This slow convergence rate is an inherent characteristic of the dispersive wave Eq. (4.12). In fact, if we examine the general solution (4.20) for a fixed

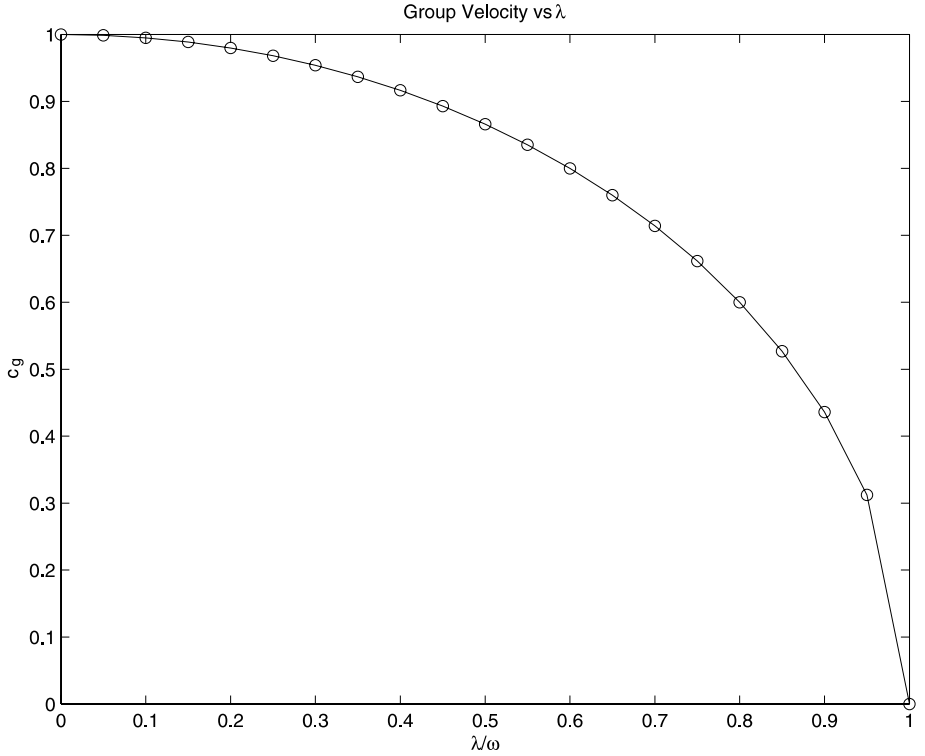

Fig. 2. The variation of the group velocity with the radial eigenvalue λ. As the parameter $\lambda/\omega \to 1$ the group velocity goes to zero. In the plane wave limit where $\lambda/\omega \to 0$ the group velocity goes to one.

$x > x_e$, the oscillatory solution is reached in the limit as $t \to \infty$. For large t, the term $J_0(\lambda_{mn}\sqrt{(t-t')^2 - (x-x_e)^2})$ decays like $1/\sqrt{\lambda_{mn} t}$.

When k_{mn} is small, near cut-on, expansion (4.33) is valid for $\omega t \gg (\omega/k_{mn})^2$, implying a rate of convergence like $1/(c_g\sqrt{\omega t})$, where we have introduced the group velocity, $c_g = \mathrm{d}\omega/\mathrm{d}k_{mn} = k_{mn}/\omega$. This suggests that near a cut-on mode the computational time required for convergence must be such that

$$\omega t \gg \frac{1}{c_g^2}. \tag{4.34}$$

In Fig. 2, the group velocity is plotted as a function of λ_{mn}/ω and we see that as $\lambda_{mn}/\omega \to 1$, the group velocity of the waves goes to zero. In this limit, we have spinning waves in the duct and the time it takes the information at the inlet plane to pass out of the exit plane is infinite. Note we can also evaluate the integral, $I(t)$, when $k_{mn} \to 0$ and t is finite. In this case

$$I(t) \sim -\mathrm{i}k_{mn}\sqrt{\frac{2\omega t}{\pi}}\mathrm{e}^{-\mathrm{i}\omega t}. \tag{4.35}$$

Nondimensionalizing with respect to ω, this result shows that near cut-on the contribution of the nonlocal time operator is of the order of $c_g\sqrt{\omega t}$. Thus the contribution of the nonlocal operator will slowly modify the solution as time increases. It is, however, essential to obtaining the correct long time solution especially near cut-on frequencies. Local conditions such as the method of characteristics which neglect the time history of the solution will not yield accurate results.

5. Numerical implementation

In order to implement the nonreflecting boundary condition, we truncate the eigenfunction expansion for a finite number of modes (m,n)

$$p(\mathbf{x},t) = \sum_{m=-N_\theta/2}^{m=N_\theta/2-1}\sum_{n=1}^{n=N_r} p_{mn}(x,t)\,\mathrm{e}^{\mathrm{i}m\theta}R_{mn}(\rho), \tag{5.36}$$

where N_θ, N_r are the number of radial and circumferential modes needed to represent $p(\mathbf{x},t)$. Since the accuracy of the boundary condition depends on the accuracy with which we can compute each Fourier–Bessel mode at the inlet/exit boundaries, in what follows, we compare the numerical solutions to the dispersive wave equation using the nonlocal condition derived in this paper with those obtained using various local conditions [1].

5.1. Numerical implementation and discretization

In this section, we solve (4.28) using a second-order accurate scheme with the nonreflecting boundary condition (4.29) imposed at the exit. We drop the subscripts (m,n) for convenience and discretize (4.28). Using the Lax–Wendroff method, we obtain

$$\begin{aligned}\phi_i^{h+1} &= \phi_i^h + (\delta_x\phi_i^h - \lambda^2 p_i^h)\Delta t + (\delta_{xx}\phi_i^h - \lambda^2\phi_i^h)\Delta t^2/2,\\ p_i^{h+1} &= p_i^h + (\phi_i^h - \delta_x p_i^h)\Delta t + (\delta_{xx}p_i^h - \lambda^2 p_i^h)\Delta t^2/2,\end{aligned} \tag{5.37}$$

where i the spatial index and h is the time index.

The spatial derivatives are approximated with the first- and second-order central difference operators

$$\begin{aligned}\delta_x p_i^h &= (p_{i+1}^h - p_{i-1}^h)/(2\Delta x),\\ \delta_{xx} p_i^h &= (p_{i+1}^h - 2p_i^h + p_{i-1}^h)/(\Delta x^2).\end{aligned} \tag{5.38}$$

Using the trapezoidal rule to evaluate the continuous nonreflecting boundary conditions, Eq. (4.29), we obtain the condition

$$\phi_i^h = -\sum_{h'=1}^{N_t-2}(\kappa_i^{h'+1} + \kappa_i^{h'}), \tag{5.39}$$

where $K_i^{h'} = \phi_i^{h'} \times J_0[\lambda(t^h - t^{h'})] + \lambda p_i^{h'} J_1[\lambda(t^h - t^{h'})]$ and N_t is the number of timesteps

At the inlet we impose incident acoustic disturbances. The incident disturbance is expressed

$$p^{\mathrm{I}}(t) = \sum_{l=1}^{n} a_l^+ \, \mathrm{e}^{-\mathrm{i}\omega_l t}, \tag{5.40}$$

where l is the index of each acoustic wave with amplitude, a_l^+, and frequency, ω_l, that propagates into the domain and the inlet plane lies in the axial plane, $x_{\mathrm{i}} = 0$. The nonreflecting boundary condition at the inlet is then

$$\psi_i^h = -\sum_{h'=1}^{N_t-2}(\gamma_i^{h'+1} + \gamma_i^{h'}), \tag{5.41}$$

where $\psi_i^h = (\frac{\partial}{\partial t} - \frac{\partial}{\partial x})(p_i^h - p^I)$, $\gamma_i^{h'} = \psi_i^{h'} \times J_0[\lambda(t^h - t^{h'})] + \lambda(p_i^{h'} - p^I)J_1[\lambda(t^h - t^{h'})]$.

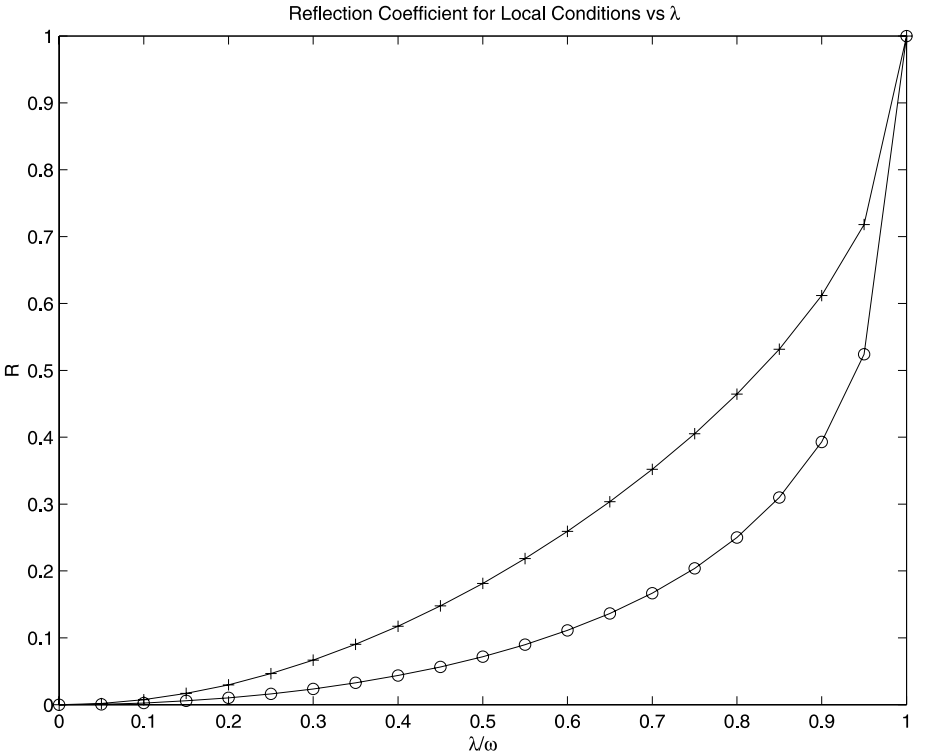

Fig. 3. The reflection coefficients for the local boundary conditions, $BC1$ and $BC2$ as a function of the parameter λ/ω.

5.1.1. Local boundary conditions

In order to examine the performance of the exact boundary condition, we implement several local boundary conditions at the exit plane and compare the solutions for various values of the parameter λ. Two commonly used local conditions are

$$\phi(x,t) = 0 \tag{5.42}$$

and

$$\frac{\partial \phi}{\partial t} - \lambda^2 p = 0. \tag{5.43}$$

These conditions will be referred to as BC1 and BC2 in the remainder of the text. They were derived in [1] by making approximations in the limit $\lambda/\omega \ll 1$. Fig. 3 shows the reflection coefficient, R, for $BC1$ and $BC2$

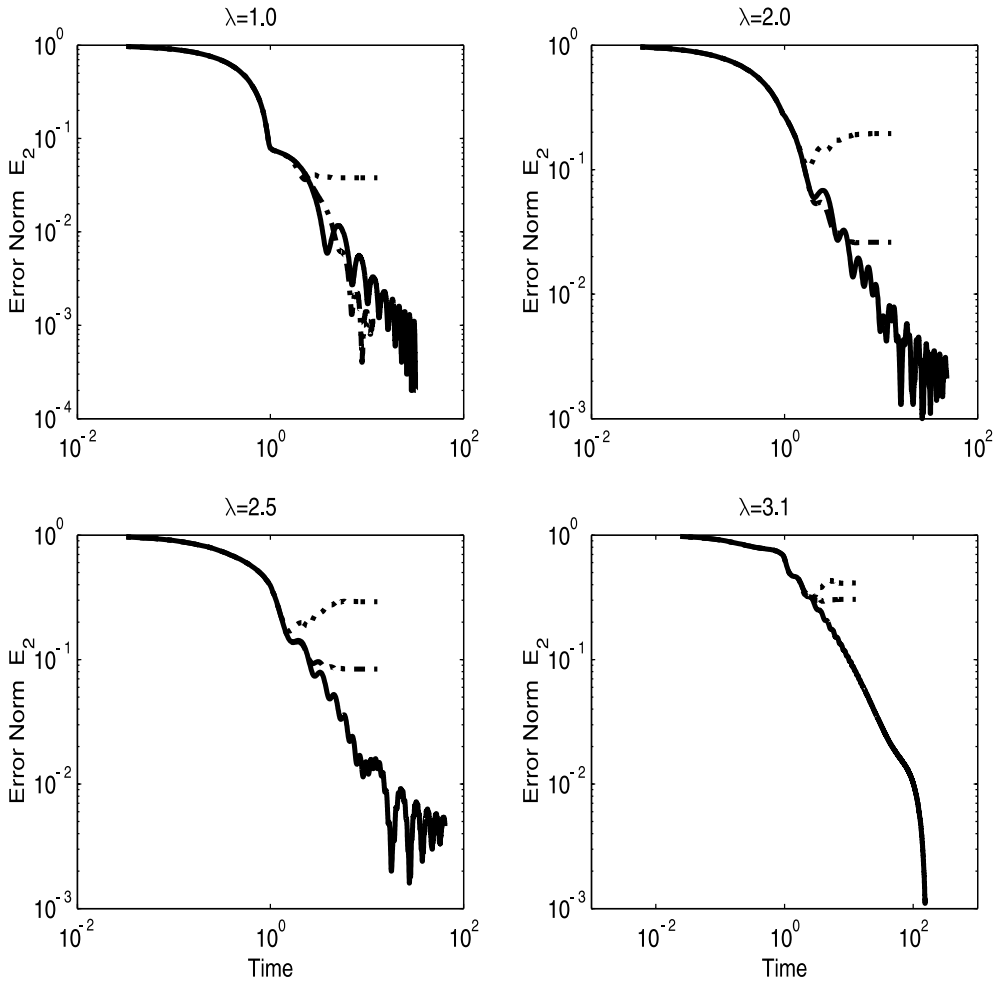

Fig. 4. The time-dependent error is plotted as a function of time. The error is a measure of the difference between the long-time analytic solution and the numerical solution. Each figure corresponds to the error convergence for different values of the parameter, λ and $\omega = \pi$. The dotted curve, dot-dashed curve and the solid curve correspond to the error convergence for the numerical solution with $BC1, BC2$ and the nonlocal boundary condition, respectively.

where the reflection coefficient is defined as the ratio of the amplitude of the reflected and incident waves. Note that as $\lambda/\omega \to 1$ both conditions become perfectly reflecting and in the limit $\lambda/\omega \to 0$ both conditions are perfectly nonreflecting. The higher order accurate boundary condition $BC2$ has a smaller reflection coefficient over a larger portion of the parameter space λ/ω.

6. Numerical results

In this section, we impose several different types of incident waves using three different exit boundary conditions. The exact boundary condition, (4.29), and the two local boundary conditions (5.42), (5.43) which we refer to as $BC1$ and $BC2$, respectively. At the inlet, we assume that no physical reflections occur and thus impose, $p = p^{\mathrm{I}}(t)$. The initial condition is chosen to be $p(x,0) = 0$ and $\partial p/\partial t = 0$. We consider three different incident disturbances: (i) a case with a single acoustic wave where the long-time solution is time-periodic, (ii) a case with multiple acoustic waves where the solution is time-periodic and (iii) a case

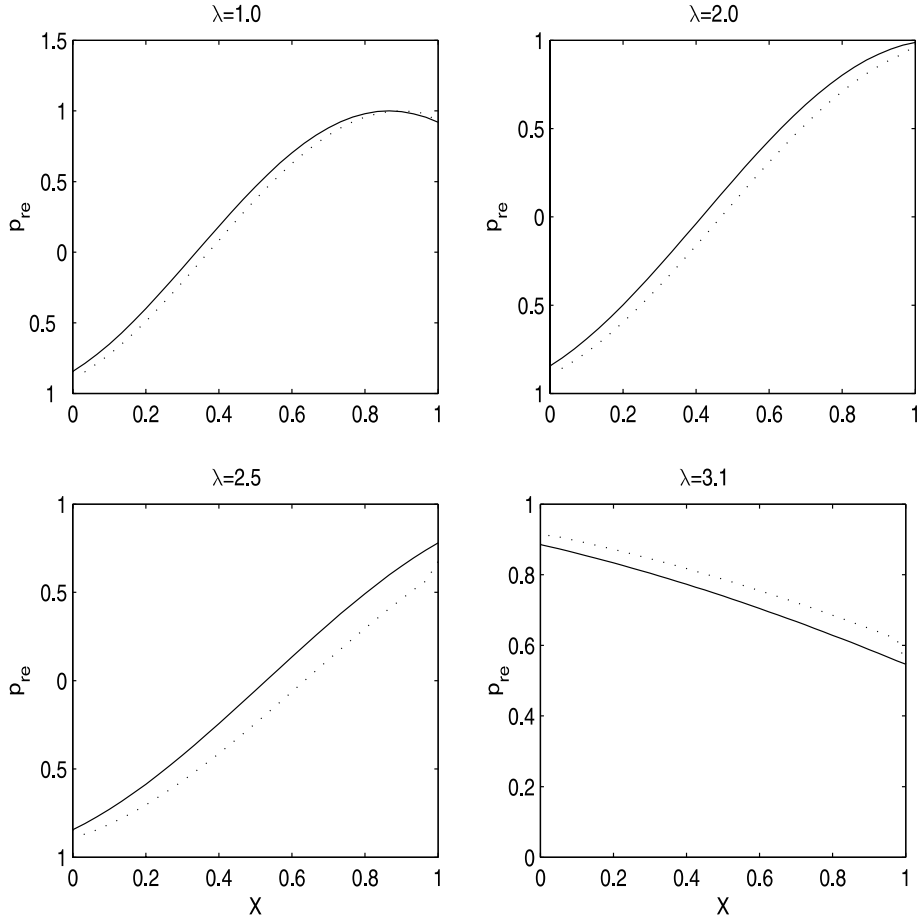

Fig. 5. The real part of the long-time numerical solution and the exact time-periodic solution is plotted in the domain. Each figure shows the solution for different values of the parameter, λ and $\omega = \pi$. The dotted curve corresponds to the numerical solution with the nonlocal boundary condition and the solid curve corresponds to the exact time-periodic solution.

with multiple acoustic waves where the long-time solution is nearly periodic. To obtain a measure of the convergence of the numerical scheme to the long-time exact solution, we define the time-dependent error over the spatial domain as

$$E(t) = \sum_{i=1}^{i=N} \frac{\|p_i^e - p_i^h\|}{\|p_i^e\|} \Big/ N, \tag{6.44}$$

where N denotes the number of points in the computational domain and p_i^e is the exact long-time solution in the domain.

6.1. Time-periodic waves

We impose time-periodic waves, characterized by the frequency, ω, at the inlet plane and the number of points in the computational domain is $N = 41$. In the first case, we propagate a single harmonic wave into

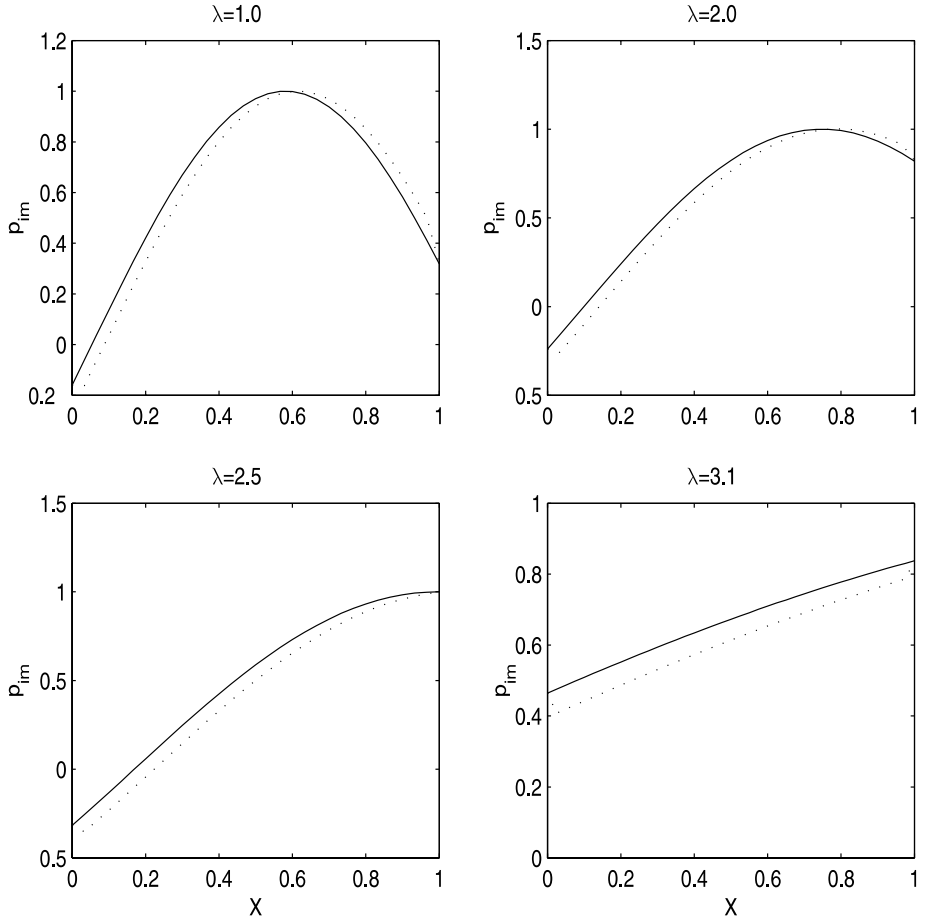

Fig. 6. The imaginary part of the long-time numerical solution and the exact time-periodic solution is plotted in the domain. Each figure shows the solution for different values of the parameter, λ and $\omega = \pi$. The dotted curve corresponds to the numerical solution with the nonlocal boundary condition and the solid curve corresponds to the exact time-periodic solution.

the domain with an angular frequency, $\omega = \pi$ and consider four different problems with $\lambda = 1.0, 2.0, 2.5, 3.1$. Note that for $\lambda = 3.1$ both $BC1$ and $BC2$ are highly reflective. In Fig. 4, we plot the time-dependent global error versus time for each of the three boundary conditions and values of the parameter λ. In the top left corner, $\lambda = 1.0$ and the performance of $BC2$ is comparable to the exact condition in the limit as t becomes large. However, as λ increases the exact condition shows a marked improvement over the local conditions and the error is an order of magnitude smaller using the exact condition for $\lambda = 2.5, 3.1$. Note also that as λ increases the group velocity of the wave decreases and the results indicate that the time needed to reach the time-periodic solution increases. This is consistent with the asymptotic analysis in Section 4.2.

In Figs. 5 and 6 we present the real and imaginary parts of the solution for various values of λ. The solid line denotes the exact solution and the dotted line denotes the numerical solution at $t = t_{\text{final}}$ using the exact boundary condition where t_{final} is determined based on the convergence of the numerical solution to the time periodic solution. For all values of λ, the agreement between the exact solution and the numerical

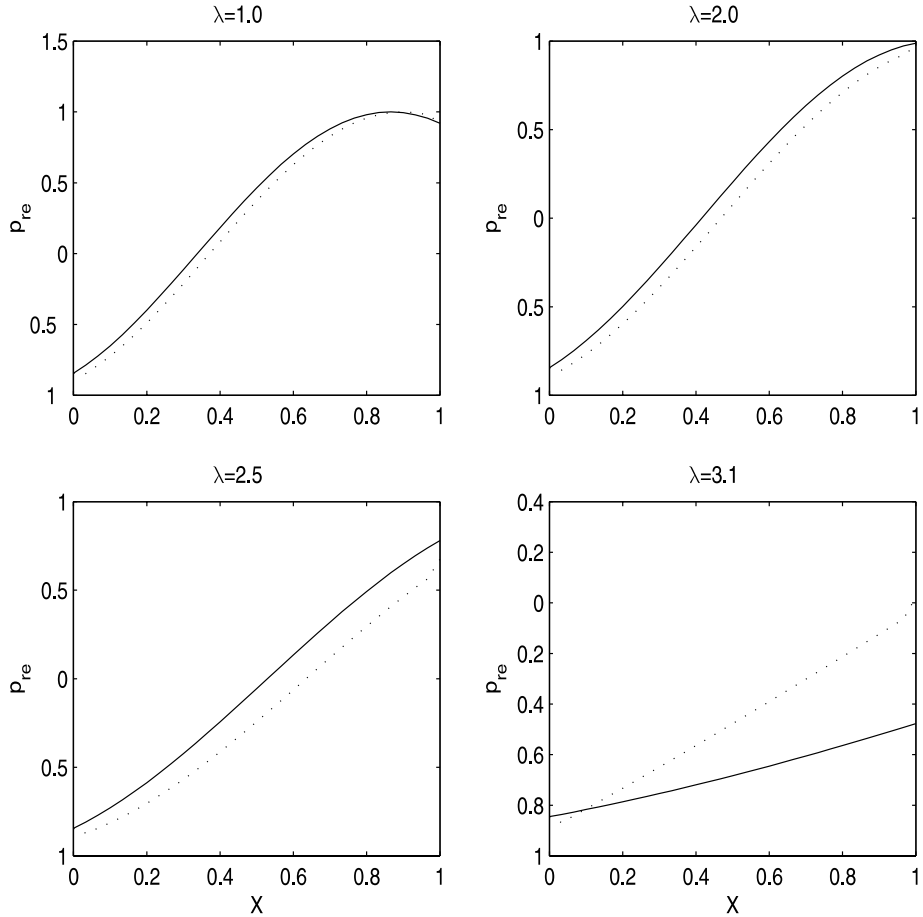

Fig. 7. The real part of the long-time numerical solution and the exact time-periodic solution is plotted in the domain. Each figure shows the solution for different values of the parameter, λ and $\omega = \pi$. The dotted curve corresponds to the numerical solution with the local boundary condition, $BC2$, and the solid curve corresponds to the exact time-periodic solution.

solution is quite good. Note that the solution for $\lambda = 3.1$ varies slowly in x and is thus nonlocal. The largest error is observed at the inlet and exit of the domain.

In Figs. 7 and 8, we present the real and imaginary parts of the numerical and exact solution for various values of λ. The solid line denotes the exact solution and the dotted line denotes the numerical solution using the local boundary condition $BC2$ at $t = t_{\text{final}}$. For small values of λ, the agreement between the exact solution and the numerical solution is quite good. However, some discrepancy between the exact and numerical solution is observed for $\lambda = 2.5$ and a significant error is observed for $\lambda = 3.1$.

Many problems are characterized by several dominant frequencies. In order to test the boundary conditions for this class of problems, we impose an inlet forcing consisting of three time-periodic waves with frequencies, $\omega = \pi, 1.2\pi$, and 2π. We examine the effect of the parameter λ on the numerical solution using $BC2$ and the nonlocal boundary condition.

In Fig. 9(a)–(c), we show the time-dependent error and the real and imaginary parts of the solution for $\lambda = 2$. In Fig. 9(a) the solid curve denotes the error using the exact boundary condition and the dotted curve

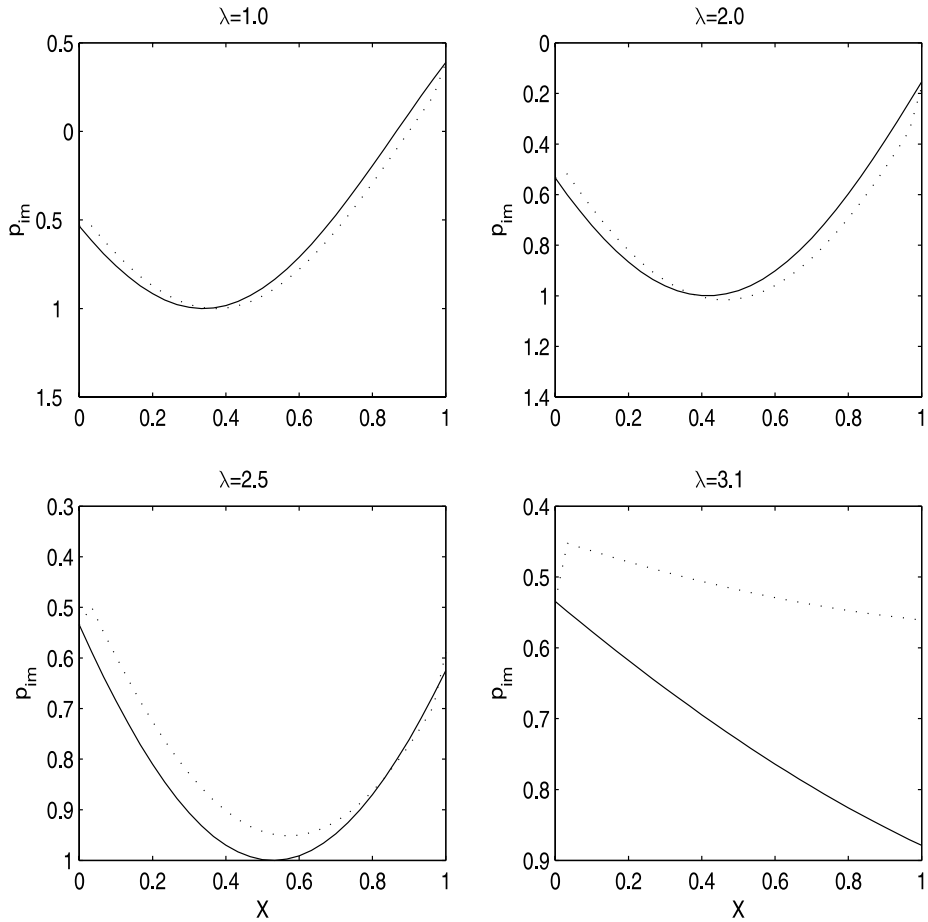

Fig. 8. The imaginary part of the long-time numerical solution and the exact time-periodic solution is plotted in the domain. Each figure shows the solution for different values of the parameter, λ and $\omega = \pi$. The dotted curve corresponds to the numerical solution with the local boundary condition, $BC2$ and the solid curve corresponds to the exact time-periodic solution.

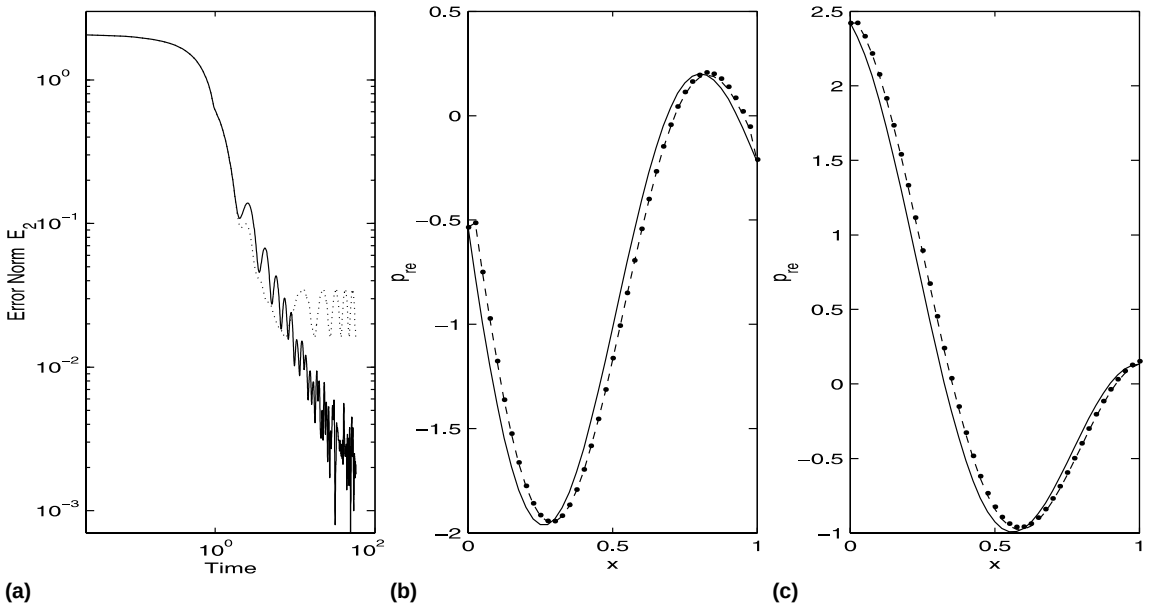

Fig. 9. The frequencies of each of the waves are $\omega = \pi, 1.2\pi$ and 2π. In each of the figures $\lambda = 2.0$. (a) In the left-most column, the time-dependent error is plotted as a function of time. The solid and dotted curves correspond to the error using $BC2$ and the exact boundary condition, respectively. (b) The middle column shows the real part of the exact solution, the numerical solution with $BC2$ and the numerical solution with the exact boundary condition. The exact solution is denoted by the solid line, the numerical solution using $BC2$ is denoted by the dots and the numerical solution with the exact boundary condition is denoted by the dashed line. (c) The right-most column shows the imaginary part of the exact solution, the numerical solution with $BC2$ and the numerical solution with the exact boundary condition. The exact solution is denoted by the solid line, the numerical solution using $BC2$ is denoted by the dots and the numerical solution with the exact boundary condition is denoted by the dashed line.

denotes the error using $BC2$. The long-time error with the exact boundary condition is approximately .002 and the error with $BC2$ is an order of magnitude larger, .02. Even though the error is much larger using $BC2$ it is still quite small. Figs. 9(b) and (c) show the real and imaginary parts of the numerical and exact solutions. The exact solution is denoted by the solid line, the numerical solution using $BC2$ is denoted by the dots and the numerical solution with the exact boundary condition is denoted by the dashed line. The agreement between the exact solution and the numerical solutions is quite good using both boundary conditions. However, slightly better agreement is observed between the numerical solution with the exact boundary condition and the exact solution.

In Figs. 10(a)–(c), we show the time-dependent error and the real and imaginary parts of the solution for $\lambda = 3.1$. In Fig. 10(a) the solid curve denotes the error using the exact boundary condition and the dotted curve denotes the error using $BC2$. Note that the rate of decrease of the error is slower than that shown in Fig. 9(a). This occurs because the group velocity of the waves is much smaller. As a result, it takes much longer for the waves at the inlet to reach the exit of the domain. The long-time error with the exact boundary condition is approximately .003 and the error with $BC2$ oscillates about a level which is several order of magnitudes larger i.e., approximately .3. Fig. 10(b)–(c) show the real and imaginary parts of the numerical and exact solutions. Again, the exact solution is denoted by the solid line, the numerical solution using $BC2$ is denoted by the dots and the numerical solution with the exact boundary condition is denoted by the dashed line. Here the difference between the numerical solution using $BC2$ and the exact boundary condition is striking. Both the amplitude and the phase of the numerical solution are significantly modified

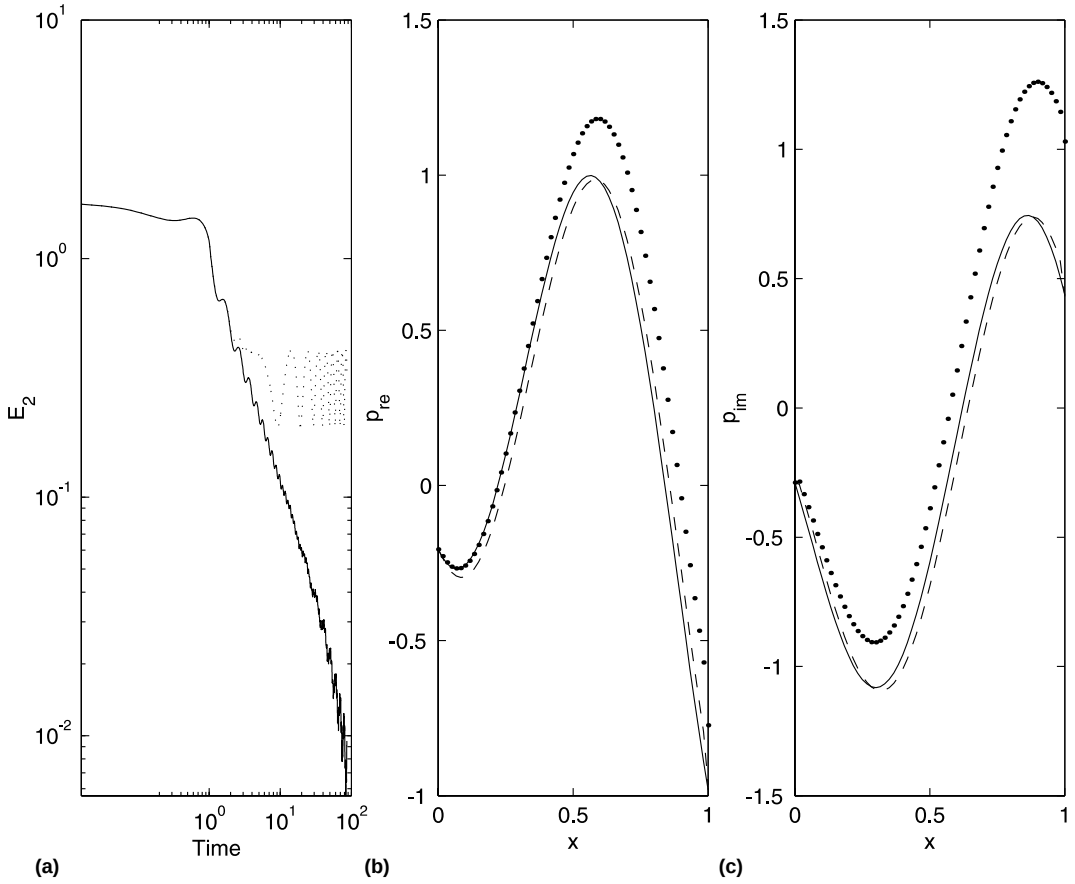

Fig. 10. The frequencies of each of the waves are $\omega = \pi, 1.2\pi$ and 2π and $\lambda = 3.1$. (a) In the left-most column, the time-dependent error is plotted as a function of time. The solid and dotted curves correspond to the error using $BC2$ and the exact boundary condition, respectively. (b) The middle column shows the real part of the exact solution, the numerical solution with $BC2$ and the numerical solution with the exact boundary condition. The exact solution is denoted by the solid line, the numerical solution using $BC2$ is denoted by the dots and the numerical solution with the exact boundary condition is denoted by the dashed line. (c) The right-most column shows the imaginary part of the exact solution, the numerical solution with $BC2$ and the numerical solution with the exact boundary condition. The exact solution is denoted by the solid line, the numerical solution using $BC2$ is denoted by the dots and the numerical solution with the exact boundary condition is denoted by the dashed line.

by the local boundary condition. In contrast, the agreement between the numerical solution using the nonlocal condition and the exact solution remains good.

6.2. Nearly periodic problems

In this section, we impose three time-periodic waves characterized by the frequencies, $\omega = \pi, \sqrt{2}\pi, \sqrt{3}\pi$ at the inlet. In this case, the waves appear to be unrelated because the ratio of the frequencies is an irrational number. We consider two different problems with $\lambda = 2.0, 3.1$ and compare the numerical solution with the exact boundary condition and $BC2$. Note that for $\lambda = 3.1$ $BC2$ is highly reflective. In Fig. 11(a)–(c), we show the time-dependent error and the real and imaginary parts of the solution for $\lambda = 2$.

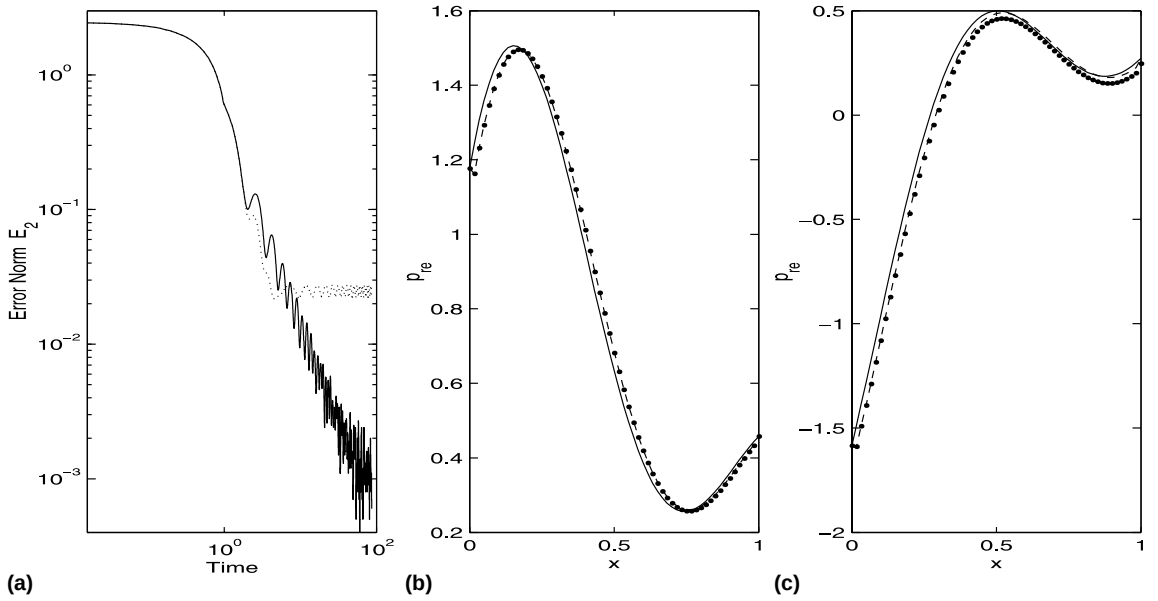

Fig. 11. The frequencies of each of the waves are $\omega = \pi, \sqrt{2}\pi$ and $\sqrt{3}\pi$. In each of the figures $\lambda = 2.0$. (a) In the left-most column, the time-dependent error is plotted as a function of time. The dotted and solid curves correspond to the error using $BC2$ and the exact boundary condition, respectively. (b) The middle column shows the real part of the exact solution, the numerical solution with $BC2$ and the numerical solution with the exact boundary condition. The exact solution is denoted by the solid line, the numerical solution using $BC2$ is denoted by the dots and the numerical solution with the exact boundary condition is denoted by the dashed line. (c) The right-most column shows the imaginary part of the exact solution, the numerical solution with $BC2$ and the numerical solution with the exact boundary condition. The exact solution is denoted by the solid line, the numerical solution using $BC2$ is denoted by the dots and the numerical solution with the exact boundary condition is denoted by the dashed line.

In Fig. 11(a) the solid curve denotes the error using the exact boundary condition and the dotted curve denotes the error using $BC2$. The long-time error with the exact boundary condition is approximately .0005 and the error with $BC2$ is nearly two orders of magnitude larger, .02. Even though the error is much larger using $BC2$ it is still quite small. One difference in the error convergence with $BC2$ is that the oscillations in error do not contain a clear period. This is due to the frequencies chosen for the inlet forcing. Fig. 11(b)–(c) show the real and imaginary parts of the numerical and exact solutions. The exact solution is denoted by the solid line, the numerical solution using $BC2$ is denoted by the dots and the numerical solution with the exact boundary condition is denoted by the dashed line. The agreement between the exact solution and the numerical solutions is quite good using both boundary conditions. However, better agreement is observed between the numerical solution with the exact boundary condition and the exact solution.

In Fig. 12(a)–(c), we show the time-dependent error and the real and imaginary parts of the solution for $\lambda = 3.1$. Again, in Fig. 12(a) the solid curve denotes the error using the exact boundary condition and the dotted curve denotes the error using $BC2$. The long-time error with the exact boundary condition is approximately .006 and the error with $BC2$ oscillates about a level which is several order of magnitudes larger i.e., approximately .3. Fig. 10(b)–(c) show the real and imaginary parts of the numerical and exact solutions. Again, the exact solution is denoted by the solid line, the numerical solution using $BC2$ is denoted by the dots and the numerical solution with the exact boundary condition is denoted by the dashed line. Here the difference between the numerical solution using $BC2$ and the exact boundary condition is clear. Even though the solution appears to be smooth at the exit, both the amplitude and the phase of the numerical

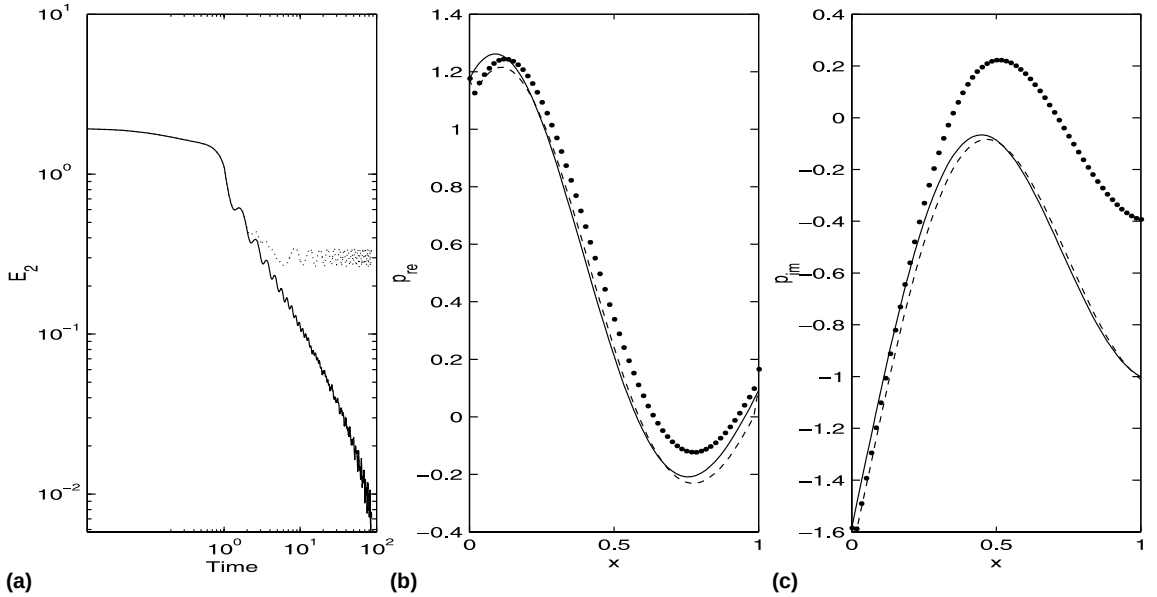

Fig. 12. The frequencies of each of the waves are $\omega = \pi, \sqrt{2}\pi$ and $\sqrt{3}\pi$. In each of the figures $\lambda = 3.1$. (a) In the left-most column, the time-dependent error is plotted as a function of time. The dotted and solid curves correspond to the error using *BC*2 and the exact boundary condition, respectively. (b) The middle column shows the real part of the exact solution, the numerical solution with *BC*2 and the numerical solution with the exact boundary condition. The exact solution is denoted by the solid line, the numerical solution using *BC*2 is denoted by the dots and the numerical solution with the exact boundary condition is denoted by the dashed line. (c) The right-most column shows the imaginary part of the exact solution, the numerical solution with *BC*2 and the numerical solution with the exact boundary condition. The exact solution is denoted by the solid line, the numerical solution using *BC*2 is denoted by the dots and the numerical solution with the exact boundary condition is denoted by the dashed line.

solution are significantly modified by the local boundary condition. In contrast, the agreement between the numerical solution using the nonlocal condition and the exact solution remains good.

7. Conclusions

An exact nonreflecting boundary condition is derived and tested for several classes of time-dependent dispersive wave problems. The boundary condition exploits the result that in most problems of interest only a finite number of waves carry acoustic energy to the far-field. As a result, an exact boundary condition which is local in space but nonlocal in time is derived. Excellent agreement between the exact solution and the numerical solution is obtained for incident waves with a wide range of incident angles to the exit boundary. The numerical results for time-periodic waves are consistent with the asymptotic analysis which shows that the rate of convergence of the numerical solution to a periodic solution decreases as the group velocity of the wave decreases. The excellent numerical results for various incident waves suggest that these boundary conditions can be accurately applied to various applications ranging from tonal and broadband noise to ultrasonics. Moreover, the use of local conditions is limited to problems where the group velocity is $O(1)$. Unfortunately, in problems where the incident wave interacts or is scattered by a body the group velocity of the waves at the boundary is not known a priori and the exact boundary condition must be used if one wants to be certain of having small errors due to the boundary conditions. Future work will apply these boundary conditions to scattering problems.

Appendix A

Proof for Theorem 2.1. Let v_1, v_2 be the inner solutions which satisfy

$$\left(\frac{D_0^2}{Dt^2} - \nabla^2\right) v^{\pm} = f, \quad x \in [V_{\mathrm{i}} \times (0,T)]$$
$$v_{\mathrm{i}}(\vec{x},0) = \frac{\partial v_{\mathrm{i}}}{\partial t} = 0, \quad x \in V_{\mathrm{i}}, \tag{A.1}$$

and the boundary condition for each mode, (4.29), where V_{i} is the inner volume, f is a source term representing inhomogeneities in the inner domain and $i = 1,2$. Let p_i be the unique outer solutions in v of ((2.1)–(2.3)) with the boundary condition

$$v_{\mathrm{i}}^{\pm} = p_i^{\pm} \tag{A.2}$$

on $x = x_{\mathrm{e}}, x_{\mathrm{i}}$, where the plus (minus) denotes the exit (inlet) boundary of the inner domain, respectively. Let $w_i = p_i$ in V and $w_i = v_i$ in V_{i}. Then by (A.2), w_{i} is continuous across the inflow/outflow boundaries, $x = x_{\mathrm{i}}, x_{\mathrm{e}}$ as are its time, tangential and radial derivatives. Since $v_{\mathrm{i}}, p_{\mathrm{i}}$ satisfy a second-order equation, it suffices to show that the normal derivative of w_i is continuous across the inflow/outflow boundary to show that w_i is a smooth solution of (A.1). Since $p_{\mathrm{i}} = v_{\mathrm{i}}$ at $x = x_{\mathrm{i}}, x_{\mathrm{e}}$, then

$$\int_0^t \left[\left(\frac{\partial p_{\mathrm{i}}^{\pm}}{\partial t} \pm \frac{\partial p_{\mathrm{i}}^{\pm}}{\partial x}\right) J_0(\lambda^{\pm}(t-t'))\right] \mathrm{d}t' = \int_0^t \left[\left(\frac{\partial v_{\mathrm{i}}^{\pm}}{\partial t} \pm \frac{\partial v_{\mathrm{i}}^{\pm}}{\partial x}\right) J_0(\lambda^{\pm}(t-t'))\right] \mathrm{d}t'. \tag{A.3}$$

By continuity of $\frac{\partial p_{\mathrm{i}}^{\pm}}{\partial t}$ on $x_{\mathrm{e}}, x_{\mathrm{i}}$ then $\frac{\partial p_{\mathrm{i}}^{\pm}}{\partial x} = \frac{\partial v_{\mathrm{i}}^{\pm}}{\partial x}$. Thus the normal derivative of w_{i} is continuous on $x_{\mathrm{i}}, x_{\mathrm{e}}$. This implies that w_1, w_2 are smooth solutions of the initial boundary value problem in the infinite domain. Thus, if the infinite domain problem has a unique solution, $w_1 = w_2$, completing the proof. □

Appendix B

In this appendix, we use the method of stationary phase to derive the long time solution of the integral

$$I(t,\lambda_{mn},\omega) = \lambda_{mn}\sqrt{\omega^2 - \lambda_{mn}^2} \int_0^t \mathrm{e}^{-\mathrm{i}\omega t'} J_1[\lambda_{mn}(t-t')]\,\mathrm{d}t'. \tag{B.1}$$

Using the integral form of the Bessel function,

$$J_1(\lambda_{mn}(t-t')) = \frac{1}{2\pi}\int_{-\pi}^{\pi} \mathrm{e}^{\mathrm{i}(-\theta+\lambda_{mn}(t-t')\sin\theta)}\,\mathrm{d}\theta. \tag{B.2}$$

Eq. (B.1) becomes

$$I(t,\omega,\lambda_{mn}) = \frac{\lambda_{mn}\sqrt{\omega^2-\lambda_{mn}^2}}{2\pi}\int_{-\pi}^{\pi} \mathrm{e}^{\mathrm{i}(-\theta+\lambda_{mn}t\sin\theta)} \int_0^t \mathrm{e}^{\mathrm{i}(-\omega-\lambda_{mn}\sin\theta)t'}\,\mathrm{d}t'\,\mathrm{d}\theta. \tag{B.3}$$

Integrating with respect to $\mathrm{d}t'$, we obtain

$$I(t,\omega,\lambda_{mn}) = \left\{\frac{-1}{2\pi i}\int_{-\pi}^{\pi} \frac{\mathrm{e}^{-\mathrm{i}(\omega t+\theta)}}{\omega+\lambda_{mn}\sin\theta}\,\mathrm{d}\theta + \frac{1}{2\pi i}\int_{-\pi}^{\pi} \frac{\mathrm{e}^{\mathrm{i}(\lambda_{mn}t\sin\theta-\theta)}}{\omega+\lambda_{mn}\sin\theta}\,\mathrm{d}\theta\right\}\lambda_{mn}\sqrt{\omega^2-\lambda_{mn}^2}. \tag{B.4}$$

The first integral in (B.4), $I_1(t)$, can be evaluated exactly and is given by

$$I_1(t) = \left(\sqrt{\omega^2 - \lambda_{mn}^2} - \omega\right) \mathrm{e}^{-\mathrm{i}\omega t}. \tag{B.5}$$

The second integral for large $\lambda_{mn}t$, denoted $I_2(t)$, can be evaluated using the method of stationary phase. Note that there are two stationary phase points $\pi/2$ and $-\pi/2$. Thus we have for the limit $\lambda_{mn}t \gg 1$,

$$I_2(t) = \sqrt{\frac{2}{\pi\lambda_{mn}t}} \frac{\lambda_{mn}}{\sqrt{\omega^2 - \lambda_{mn}^2}} [\lambda_{mn}\cos(\lambda_{mn}t - \pi/4) - \mathrm{i}\omega\sin(\lambda_{mn}t - \pi/4)] + \mathrm{O}\left(\frac{1}{\lambda_{mn}t}\right). \tag{B.6}$$

References

[1] B. Engquist, A. Majda, Absorbing boundary conditions for the numerical simulation of waves, Math. Comput. 31 (1977) 629–651.
[2] B. Engquist, A. Majda, Radiation boundary conditions for acoustic and elastic wave calculations, Commun. Pure Appl. Math. 32 (1979) 313–357.
[3] A. Bayliss, E. Turkel, Radiation boundary conditions for wave-like equations, Commun. Pure Appl. Math. 33 (1980) 707–725.
[4] K. Thompson, Time-dependent boundary conditions for hyperbolic systems, J. Comp. Phys. 68 (1987) 1–24.
[5] K. Thompson, Time-dependent boundary conditions for hyperbolic systems. II, J. Comp. Phys. 89 (1990) 439–461.
[6] M.J. Grote, J.B. Keller, Exact nonreflecting boundary conditions for the time-dependent wave equation, SIAM J. Appl. Math. 55 (1995) 280–297.
[7] D. Givoli, J.B. Keller, Nonreflecting boundary conditions for elastic waves, Wave Motion 12 (1990) 261–279.
[8] M.B. Giles, Nonreflecting boundary conditions for the Euler equations, AIAA J. 28 (1990) 2050–2058.
[9] J. Fang, H.M. Atassi, Compressible flows with vortical disturbances around a cascade of loaded airfoils, in: H.M. Atassi (Ed.), Unsteady Aerodynamics, Aeroacoustics and Aeroelasticity of Turbomachines and Propellers, Springer, Berlin, 1991, pp. 149–176.
[10] J.W. Goodrich, T. Hagstrom, Accurate algorithms and radiation boundary conditions for linearized Euler equations, AIAA Paper (1996) 96-1660.
[11] Higdon, L. Robert, Absorbing boundary conditions for difference approximations to the multi-dimensional wave equation, Math. Comput. 47 (1986) 437–459.
[12] T. Colonius, numerically nonreflecting boundary and interface conditions for compressible flow and aeroacoustic computations, AIAA J. 35 (1997) 1126–1133.
[13] C.W. Rowley, T. Colonius, J. Comp. Phys. 157 (2001) 500–538.
[14] J.W. Goodrich, T. Hagstrom, A comparison of two accurate boundary treatments for computational aeroacoustics, AIAA Paper (1997) 97-1585.
[15] O.V. Atassi, A. Ali, Inflow/Outflow conditions for internal time-harmonic Euler equations, J. Comp. Acoustics 10 (2002) 155–182.
[16] R. Courant, D. Hilbert, Meth. Math. Phys. (1937).
[17] G.N. Watson, A Treatise on the Theory of Bessel Functions, second ed. (1966).
[18] T. Hagstrom, Radiation boundary conditions for the numerical simulation of waves, Acta Num. 8 (1999) 47–106.
[19] T. Hagstrom, H. Goodrich, Accurate radiation boundary conditions for the linearized Euler equations in cartesian domains, SIAM J. Sci. Comput. 24 (2002) 770–795.
[20] B. Alpert, L. Greengard, T. Hagstrom, J. Comp. Phys. 180 (2002) 270–296.
[21] C. Lubich, A. Schadle, Fast convolution for nonreflecting boundary conditions, SIAM J. Sci. Comp. 24 (2002) 161–182.
[22] M.J. Grote, J.B. Keller, Nonreflecting Boundary Conditions for Time-Dependent Scattering, J. Comput. Phys. 127 (1996) 52–65.